Designing highly delocalized solitons by harnessing the structural parity of π-conjugated polymers

Kalyan Biswas, Jesús Janeiro, Aurelio Gallardo, Marco Lozano, Ana Barragán, Berta Álvarez, Diego Soler-Polo, Oleksandr Stetsovych, Andrés Pinar Solé, Koen Lauwaet, José M. Gallego, Dolores Pérez, Rodolfo Miranda, José I. Urgel, Pavel Jelínek, Diego Peña & David Écija

To cite this version

Biswas, K., Janeiro, J., Gallardo, A. et al. Designing highly delocalized solitons by harnessing the structural parity of π-conjugated polymers (2024). https://hdl.handle.net/20.500.12614/3807

Designing highly delocalized solitons by harnessing the structural parity of π-conjugated polymers

Kalyan Biswas[1], Jesús Janeiro[2], Aurelio Gallardo[1,3], Marco Lozano[3], Ana Barragán[1], Berta Álvarez[2], Diego Soler-Polo[3], Oleksandr Stetsovych[3], Andrés Pinar Solé[3], Koen Lauwaet[1], José M. Gallego[4], Dolores Pérez[2], Rodolfo Miranda[1], José I. Urgel*[,1], Pavel Jelínek*[,3], Diego Peña*[,2] and David Écija*[,1]

[1]IMDEA Nanoscience, C/ Faraday 9, Campus de Cantoblanco, 28049 Madrid, Spain
[2]Centro Singular de Investigación en Química Biolóxica e Materiais Moleculares (CiQUS) and Departamento de Química Orgánica, Universidade de Santiago de Compostela, 15782 Santiago de Compostela, Spain
[3]Institute of Physics of the Czech Academy of Science, CZ-16253 Praha, Czech Republic
[4]Instituto de Ciencia de Materiales de Madrid (ICMM), CSIC, Cantoblanco, 28049 Madrid, Spain

* Address correspondence to these authors

Abstract

π-Conjugated polymers are a class of materials featuring an alternation of single and double bonds along their backbone, which enables delocalized π-electrons. Their unique electronic structure makes them vital in applications like organic electronics, solar cells, and light-emitting diodes. A key feature in such materials is the emergence of topological quasiparticles, termed solitons, which are crucial for their observed high electrical conductivity.

By using on-surface synthesis, we present a chemical reaction based on the regio- and stereoselective coupling of indenyl moieties for fabricating π-conjugated acenoindenylidene polymers on Au(111) surface, which feature a longitudinal polyacetylene backbone. The relationship between structural parity and electronic properties is investigated. We discover that odd-membered polymers exhibit an in-gap soliton state, which, owing to their low bandgaps, spatially extends several nanometers along the longitudinal polyacetylene backbone. Our findings pave the way for the design of π-conjugated polymers that are able to host intrinsic solitons through chemical design by exploiting structural parity, without the need for external doping.

∏-conjugated polymers are composed of an alternating arrangement of single and double bonds that facilitates high delocalization of electrons along the polymer backbone[1-3]. Herein, the emergence of freely-propagating topological domain-wall states, so-called solitons, are key for the observed high electrical conductivity, and maximizing the delocalization of the soliton over the molecular backbone is sought to enhance such conductivity[1-3].

Nowadays, the design of π-conjugated polymers lies at the heart of materials science, given their scientific and technological interest across fields such as optoelectronics, photovoltaics, spintronics, sensing, and energy storage[2,4-6]. Guided by the flexible synthetic capabilities offered by solution chemistry for tuning polymeric structure and intrinsic physico-chemical properties, enormous efforts have been, are being, and will continue to be devoted to design highly conducting polymers and comprehend the correlation between their structure and functionality. Despite remarkable synthetic progress in the field, strategies are required to overcome solubility challenges associated with the design of π-conjugated polymers. A central question is whether it is experimentally feasible to design π-conjugated polymers featuring highly delocalized solitons solely by chemical design (Figure 1a), and, thus, avoiding the need for doping. In π-conjugated polymers doping can be carried out in different routes, being harmful to the structure and stability of the polymer and energy consuming[2].

Recently, on-surface chemistry in ultra-high vacuum (UHV) conditions, known as on-surface synthesis, has emerged as a successful strategy for synthesizing carbon-based materials that were previously unattainable through traditional synthesis methods[7,8]. Following this approach, π-conjugated nanomaterials[9] such as nanographenes[10-13], 1D wires[9,14-16], graphene nanoribbons[10,17-20] or 2D sheets[21,22] could be designed. Remarkably, scanning probe microscopies that operate in UHV enable the visualization of such nanomaterials with unrivalled resolution, providing access to their electronic, magnetic, and topological characteristics at the atomic scale[23-25].

Here, we report the engineering of polymers featuring highly delocalized solitons by chemical design. By annealing a submonolayer coverage of an indenyl precursor **1** on a Au(111) surface, we report the on-surface synthesis of a π-conjugated polymer **3** (Figure 1b, where polymer **3e** and **3o** denote even-membered and odd-membered polymers, respectively). Our experimental and theoretical findings reveal that a 1D polymer featuring a polyacetylene longitudinal backbone is formed. The synthesis is enabled by a polymerization reaction based on the regio- and stereo-selective coupling of indenyl moieties involving a triple C-H cleavage from precursor **1** by metal adatoms, followed by peripheral directed homocoupling of intermediate **2**. By high-resolution scanning probe microscopy, the chemical and electronic structure of the polymer **3** is elucidated, detecting the coexistence of even- and odd-membered oligoacetylene polymers. Importantly, the structural parity of the polymer is translated into a distinct electronic structure. scanning tunneling spectroscopy (STS) complemented by density functional theory (DFT) calculations highlights the emergence of a soliton in-gap state at the Fermi level for odd-membered polymers. Owing to the low bandgap of the wires, the soliton is strongly delocalized along the longitudinal backbones of the polymer on a nanometer scale.

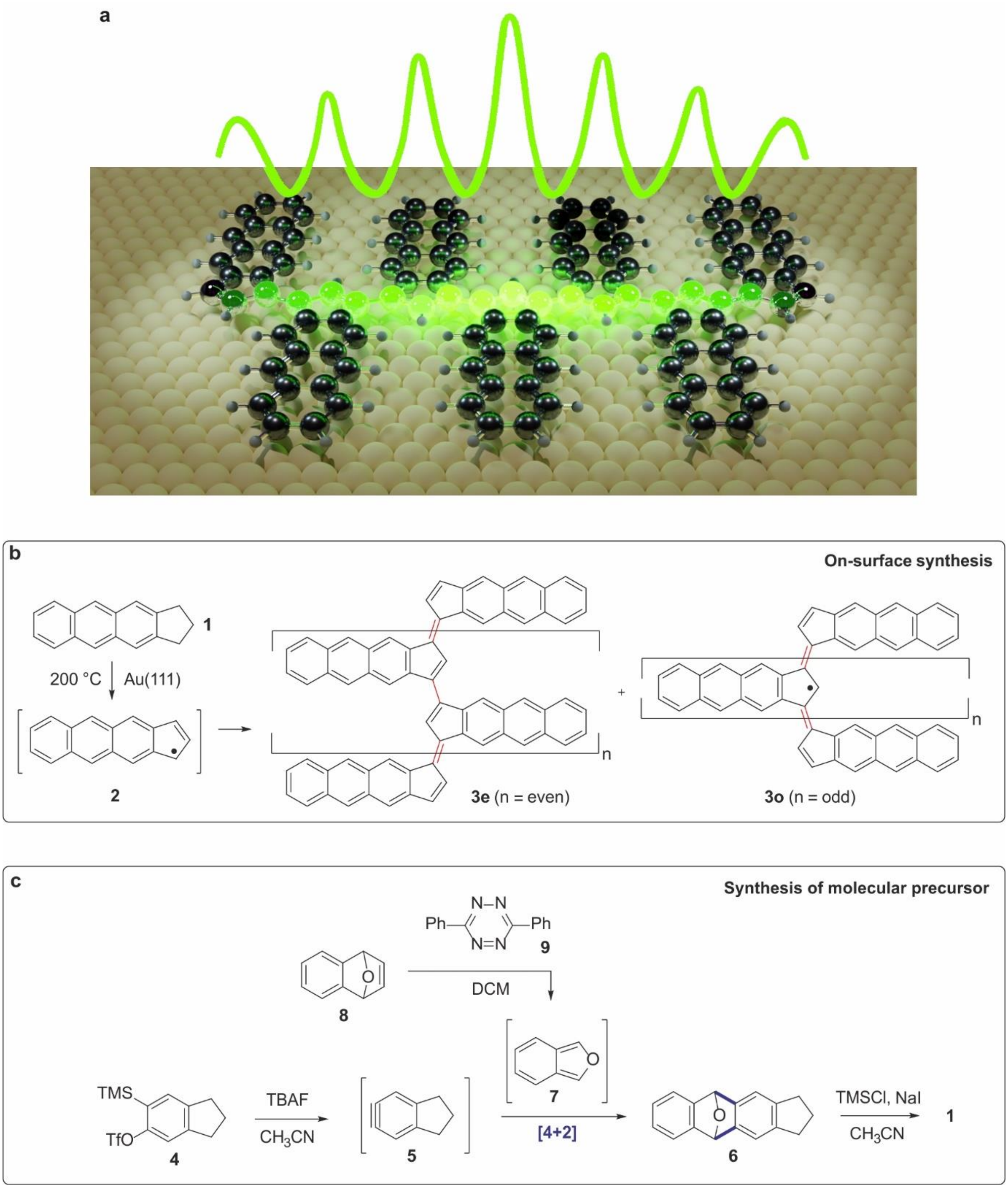

Scheme 1 | Solution synthesis of precursor 1 and on-surface synthesis of polymer 3. **a**, Delocalization of a soliton in a π-conjugated polymer simply by chemical design. **b**, Scheme of the polymerization of **1** into polymer **3** through the formation and homocoupling of intermediate **2** upon adsorption on Au(111) held at room temperature and subsequent annealing to 200 ºC. **c**, Solution synthesis of precursor **1**.

Our results report a chemical reaction to synthesize π-conjugated polymers and experimentally reveal the correlation between the structural parity and electronic properties of a polymer. Thus, we exemplify the theoretical predicted concepts of structural parity[26] as an essential factor to consider in the design of tailored nanomaterials hosting topological quasiparticles simply by chemical design. In addition, by taking advantage of the inherent low bandgaps of the synthesized polymers, we illustrate in real space the emergence and full delocalization of soliton in-gap states over polymeric backbones.

RESULTS AND DISCUSSION

Molecular precursor **1** was obtained in two steps by means of aryne chemistry in solution (Scheme 1c) [27]. First, treatment of triflate **4** with tetrabutylammonium fluoride generated highly reactive aryne **5**. This compound led to the formation of an epoxy derivative **6** by [4+2] cycloaddition with isobenzofuran **7**, which in turn was obtained by in situ treatment of compound **8** with tetrazine **9**. Finally, deoxygenation of compound **6** afforded 2,3-dihydro-1*H*-cyclopenta[*b*]anthracene (**1**), which was used for the on-surface experiments (see supporting information for synthetic and characterization details of precursor **1,** Supplementary Figures 1-3).

The sublimation of a submonolayer coverage of compound **1** under UHV conditions onto an atomically clean Au(111) surface held at room temperature gives rise to the formation of discrete supramolecular assemblies. These nanostructures, comprising from three to six intact species, are predominantly located on the FCC regions of the herringbone reconstruction (Supplementary Figure 4). A subsequent annealing step to 200 ºC induces the coupling of the precursors affording the formation of linear molecular wires (see overview scanning tunneling microscopy (STM) image in Figure 2a), which are rationalized in the following as naphthoindenylidene π-conjugated polymers (**3**), thus providing an alternative and defect-free route to engineer acenoindenylidene polymers on surfaces[28]. A minority fraction of supramolecular assemblies is still found coexisting with the polymers due to the concomitant residual gas of the precursor species upon cooling down and transferring from the preparation to the analysis chamber. Polymers of varying lengths are observed on the surface, being some of them illustrated in Figure 2b. A statistical analysis of over 400 polymers (see the histograms in Figures 2c,d and Supplementary Figure 5) reveals the presence of both even- and odd-membered wires, with the even-membered polymers being highly dominant (95%). Regarding the interaction with the substrate, the smaller polymers are all found on the FCC regions of Au(111), while the longer ones grow along the FCC regions and cross the dislocation lines in a linear fashion whenever they face an elbow[29]. The longest observed defect-free polymer comprises 86 monomers, as displayed in Figure 2e, being located from one elbow to another over a whole FCC region. Notably, the wires display some level of flexibility, enabling them to sustain open curvatures via slight bending of the polymer backbones.

Figure 2f shows a constant-current STM image of a prototype even-membered polymer **3e** comprising twelve monomers. Structural details of the polymer are accessible by non-contact atomic force microscopy (nc-AFM) measurements using a CO-functionalized tip[30,31]. Figure 2g displays the constant-height frequency-shift image of the dodecamer, in which the molecular backbone of the monomers as naphthoindenylidenes is clearly discerned. In addition, the aspect of the edges of the polymers, identical to the rims of the monomers, corroborate the –CH termination. Actually, in the few occasions that the polymers are doubly hydrogenated either at the termini or at the apex of the monomers, a bright protrusion is observed (Supplementary Figure 6), being feasible to remove such extra hydrogen by tip-induced manipulation at selected voltages[32] (Figure S7). Our structural DFT simulations reveal a bond order alternation of the linkages (Supplementary Figure 8, left panel), while our nc-AFM simulations based on such resonant form match the experimental results (Supplementary Figure 9, top panel).

A constant-current STM of a representative heptamer of the odd-membered polymers **3o** is shown in Figure 2h. Like in the even-membered counterparts, the chemical structure of the polymer can be discerned by nc-AFM imaging and its edges assigned to –CH termini (Figure 2i). Herein, the agreement with a calculated nc-AFM image for a free-standing 7-membered polymer is excellent (Supplementary Figure 9, bottom panel). Importantly, our DFT calculations reveal that there is a strong reduction of the bond length alternation between the central atoms belonging to the polyacetylene backbone (Supplementary Figure 8).

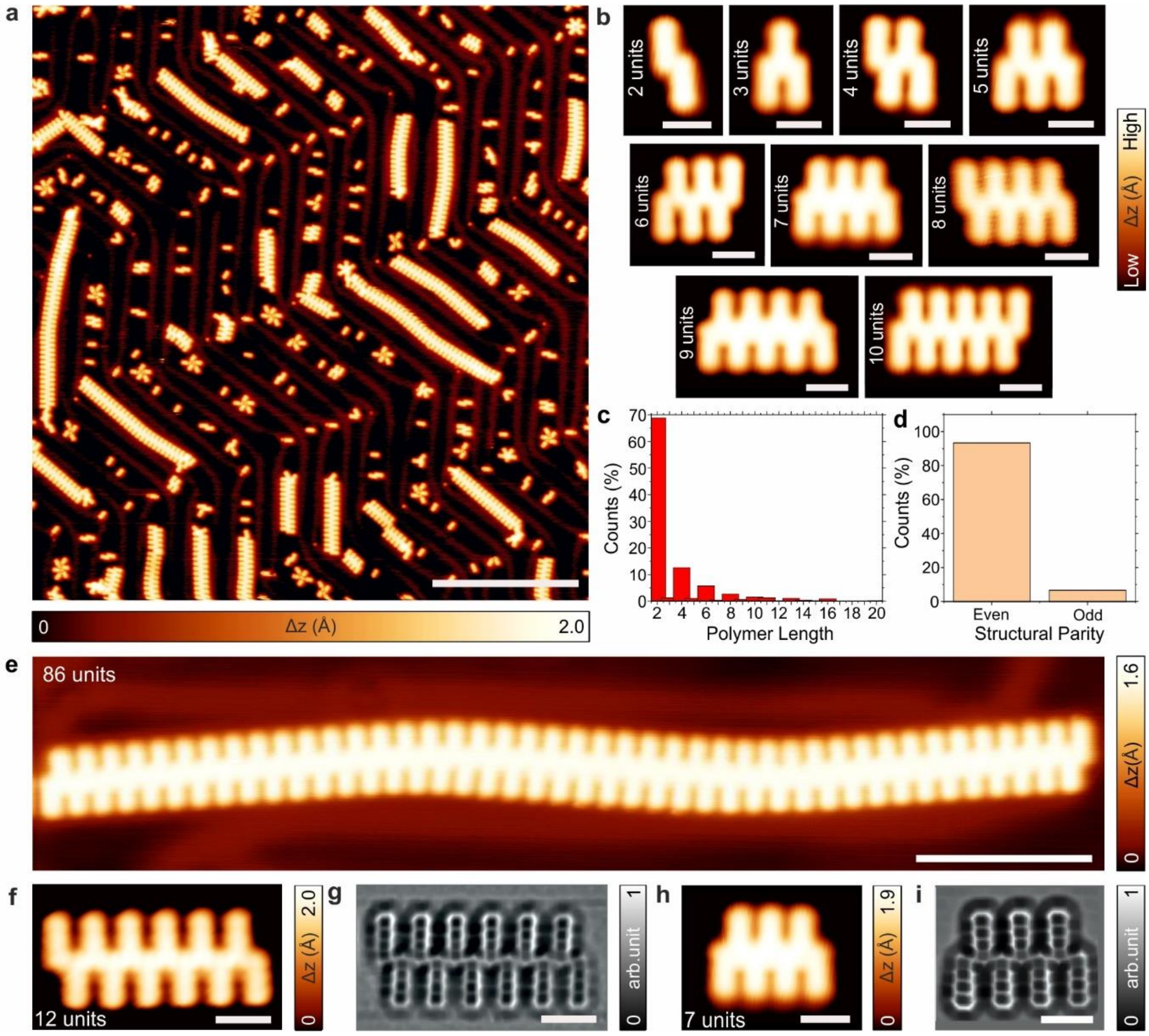

Figure 1 | On-surface synthesis of polymer 3 on Au(111). a, Overview STM image of a Au(111) surface after the deposition of a submonolayer coverage of **1** and subsequent annealing to 200 °C. V_b = 0.5 V, I_t = 10 pA, scale bar = 20 nm. **b**, Constant-current high-resolution STM images of polymers **3** with varying length acquired with a CO-functionalized tip. V_b = 50 mV, I_t = 50 pA (2 units); V_b = 0.3 V, I_t = 100 pA (3 units); V_b = 5 mV, I_t = 10 pA (4 units); V_b = -0.1 V, I_t = 70 pA (5 units); V_b = 5 mV, I_t = 10 pA (6 units); V_b = 0.5 V, I_t = 50 pA (7 units); V_b = 50 mV, I_t = 50 pA (8 units); V_b = 0.5 V, I_t = 50 pA (9 units); V_b = 5 mV, I_t = 10 pA (10 units); scale bars = 1 nm. **c-d**, Histograms of the abundance of the polymers regarding their length and structural parity, respectively. **e**, Constant-current STM image of the largest observed defect-free polymer comprising 86 monomers. V_b = 0.5 V, I_t = 50 pA, scale bar = 5 nm. **f**, High-resolution STM image, acquired with a CO-functionalized tip, of a dodecamer. V_b = 5 mV, I_t = 50 pA, scale bar = 1 nm. **g**, Constant-height frequency-shift nc-AFM image of **f** acquired with a CO-functionalized tip. V_b = 5 mV, 50 pA, scale bar = 1 nm. **h**, High-resolution STM image of an isolated heptamer. V_b = 5 mV, I_t = 50 pA, scale bar = 1 nm. **i,** Constant-height frequency-shift nc-AFM image of **h** acquired with a CO-functionalized tip. V_b = 10 mV, 50 pA, scale bar = 1 nm.

To get further insights into the reaction mechanism that originates such polymers, we carried out quantum mechanics/molecular mechanics (QM/MM) and DFT simulations[33]. We used the

QM/MM method to characterize the free-energy profile of the sequential C-H cleavage of the precursor on the surface. The polymerization process of molecular units was studied by means of the climbing image nudged elastic band (CI-NEB) DFT method[34], to make corresponding simulations computationally tractable owing to a large number of atoms.

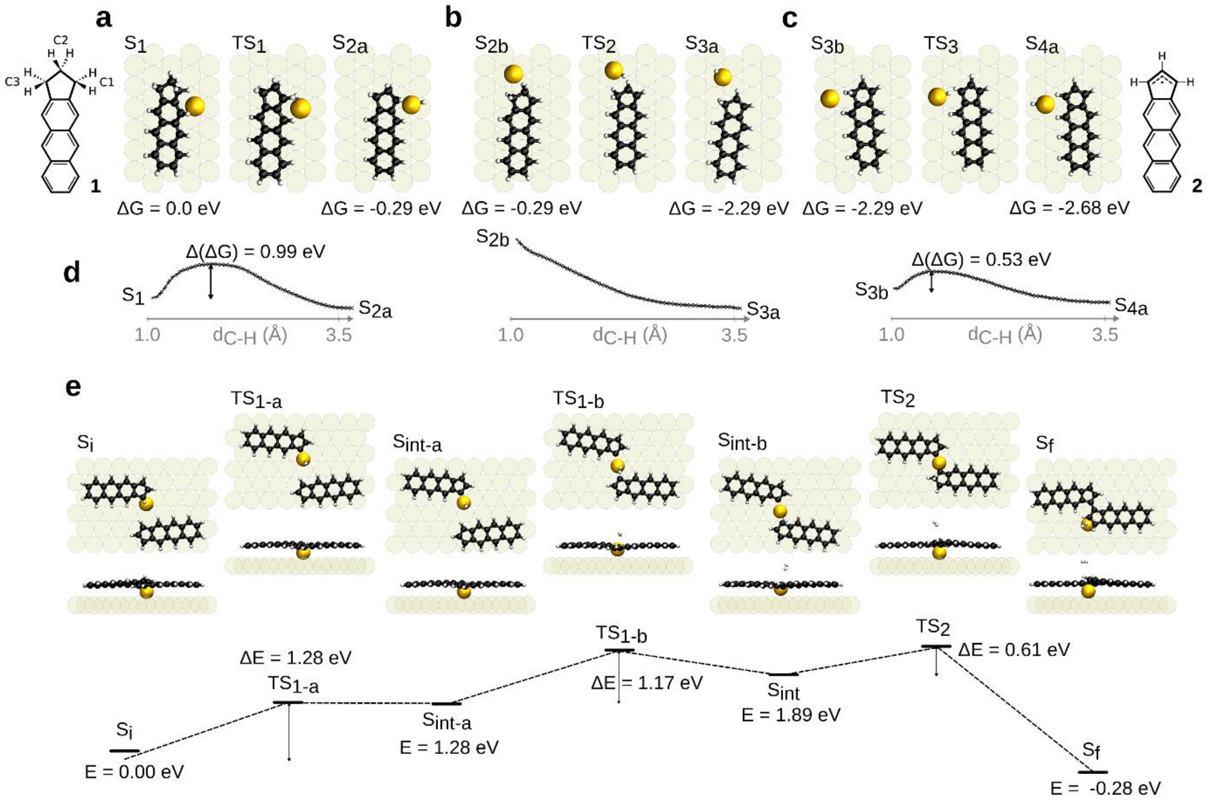

Figure 2 | Most favorable reaction pathways for the C-H cleavage of precursor **1** after its deposition and the posterior polymerization of intermediate **2**. **a**-**c**, Initial, transitional, and final structures of the three C-H cleavage processes, respectively. **d**, Concatenation of the three free energy barriers calculated for the three C-H cleavage processes. **e**, CI-NEB calculated potential energy profile for the three step-wise polymerization process found to be more favorable, and side and top view of the calculated initial (S_i), intermediate (S_{int}) final (S_f) and transitional ($TS_{1-a}, TS_{1-b}\ and\ TS_2$) states.

In the first step, we investigated the optimal sequence of the C-H cleavage processes of 2,3-dihydro-1*H*-cyclopenta[*b*]anthracene (**1**). Previously, it has been demonstrated that single adatoms may act as single-atom catalysts, substantially lowering the activation energies[35-37]. Therefore, we considered all possible C-H cleavage processes of the sp^3 carbon atoms on the five-membered ring of precursor **1** mediated by the presence of single gold adatoms, as shown in Supplementary Figure 10. Figure 3a-d displays the optimal sequence of the C-H cleavage according to the lowest activation energies obtained from free energy QM/MM simulations. We found that the first C-H cleavage on compound **1** takes place on the carbon #1 (see insert in Figure 3) of the five-membered ring having a free energy barrier of 0.99 eV. The resulting intermediate S_{2a} has energy 0.29 eV lower than the initial state (S_1). In the next step, the C-H cleavage on carbon #2 (see insert in Figure 3) at the apex of the five-membered ring in the presence of gold adatom is barrierless. The intermediate S_{3a} has lower free energy of 2.0 eV with respect to the intermediate S_{2b}. This finding is in good agreement with the fact that most of the monomers that form the polymers present the carbon #2 in the five-membered ring mono-hydrogenated. Finally, there is an additional C-H cleavage on carbon #3 of the five-membered moiety. In this case, we found an activation free energy of 0.53 eV to form a mono-hydrogenated intermediate (S_{4a}), namely intermediate **2**. This result is in good accordance with the fact that the edge of the polymers found experimentally is usually terminated with –CH rather than –CH$_2$, suggesting the molecules reach the state S_{4a} before their polymerization. Importantly, we found that additional C-H cleavage of the completely mono-hydrogenated intermediate ($S4_a$) not leading to polymerization were not thermodynamically favorable and presented very high energy barriers (Supplementary Fig. 10), suggesting that the dimerization should happen otherwise. Further details about the role of the metallic substrate in the simulations are treated in the Supporting Information (Supplementary Figs. 11-14).

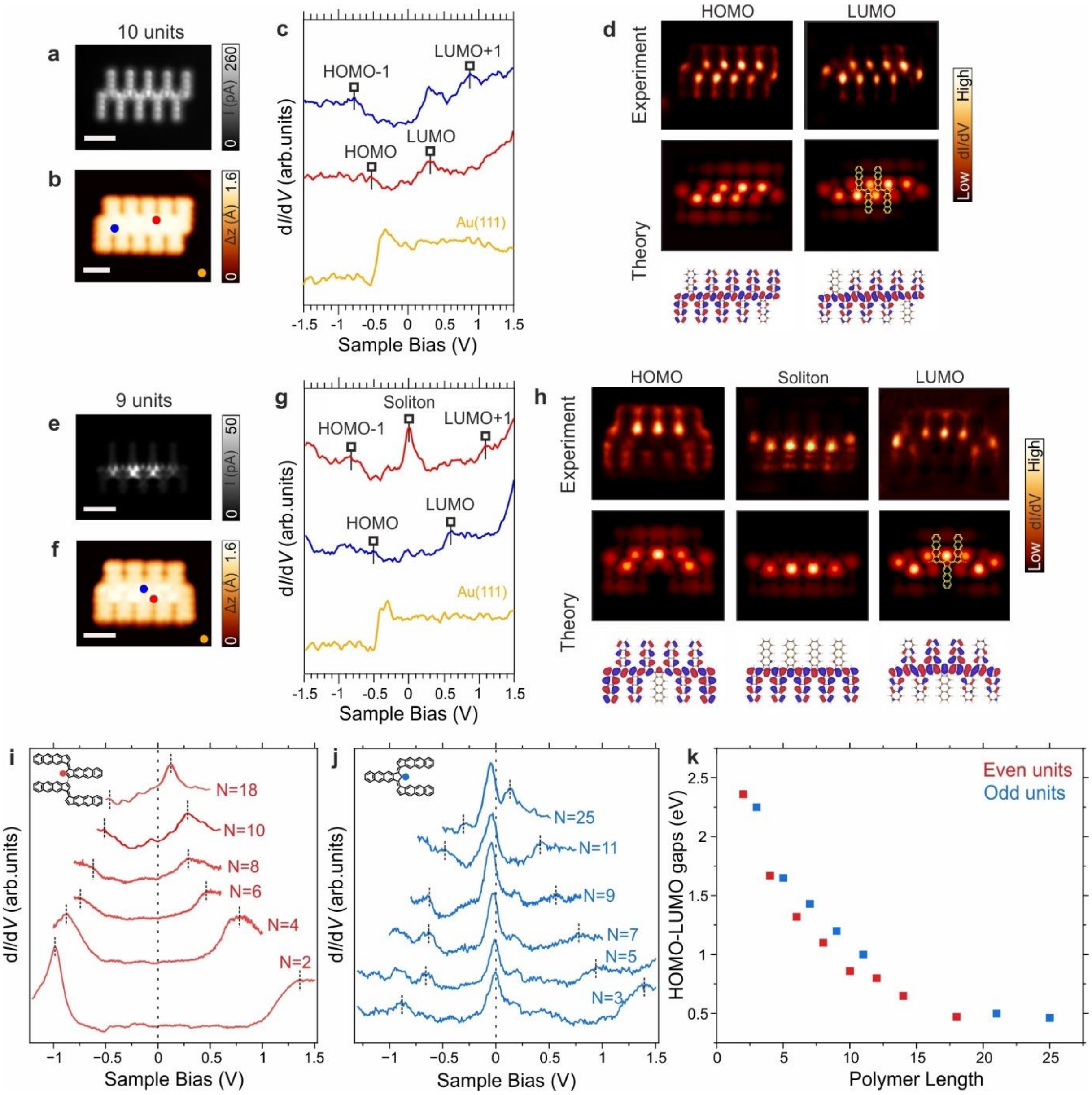

Figure 3 | Electronic structure of polymer 3 with respect to its structural parity. **a**,**e**, Constant-height high-resolution STM images of an even-membered (10-membered) and an odd-membered (9-membered) polymers acquired with a CO-functionalized tip. V_b = 5 mV, scale bars = 1 nm. **b**,**f**, High-resolution STM images of a 10-membered and 9-membered polymers acquired with a CO-functionalized tip, respectively. V_b = −2.0 V, I_t = 100 pA; scale bars = 1 nm. **c**,**g**, d*I*/d*V* spectra of 10-membered and 9-membered polymers acquired at the positions indicated by the colored circles in **b**,**f**. Reference spectra taken on the bare Au(111) surface are depicted in orange, and the acquisition position is marked with an orange circle. Open feedback parameters for d*I*/d*V* spectra: V_b = −2.0 V, I_t = 100 pA, V_{rms} = 20 mV. **d**,**h**, Top panel, experimental constant-current d*I*/d*V* maps acquired with a CO-tip. **d**, HOMO (V_b = −0.56 V, I_t = 250 pA) and LUMO (V_b = 0.25 V, I_t = 250 pA), with V_{rms} = 20 mV for a 10-membered polymer; **h**, HOMO (V_b = −0.5 V, I_t = 250 pA), Soliton (V_b = −0.10 V, I_t = 70 pA), and LUMO (V_b = 0.60 V, I_t = 250 pA), V_{rms} = 20 mV.Middle panel, corresponding DFT-calculated maps (tip-sample height = 5 Å) at the energy positions of the frontier orbitals. Bottom panel, electronic wavefunctions of the distinct states from DFT calculations. **i**,**j**, d*I*/d*V* spectra of even- and odd-membered polymers of distinct lengths, respectively. Inset: Chemical scheme showing the acquisition positions of the spectra by a colored circle. **k,** Graph displaying the evolution of HOMO-LUMO gaps of the polymers as a function of their length.

As the inclusion of another intermediate ($S4_a$) makes the system bigger and more complex, involving several additional possible reaction coordinates, turning the free energy QM/MM simulations computationally not feasible, we employed a CI-NEB DFT method to study the polymerization process of two intermediates ($S4_a$). Both QM/MM and CI-NEB methods found that the C-H cleavage at the five-membered unit is more favorable at position 1,3 than 2 (Supplementary Figures 10 and 13-16). This observation supports the highly selective growth of polymer **3**. The calculated potential energy barrier for the proposed three-step polymerization process is shown in Figure 3e. In the first step, the adatom cleavages the C-H bond on carbon #1 forming a carbene-gold complex of intermediate **2**, followed by a similar C-H cleavage in the carbon #1 of the other molecule. These two steps imply two potential energy barriers of 1.28 eV and 1.17 eV, creating a bis(carbene) gold complex. Then, as a final step, this organometallic bond evolved by extruding the gold adatom and forming a C=C double bond through an energy barrier of 0.61 eV. Note that the final product is 0.28 eV more favourable than the initial state, which makes the reaction thermodynamically stable. This mechanism can be considered an Au-catalyzed generation and dimerization of carbene derivatives. Three other alternative options for the polymerization mechanism have been considered (Supplementary Figure 15). First, we address the simultaneous C-H cleavage of two molecular units followed by the formation of molecular hydrogen and covalent C-C bond, offering an alternative polymerization process (Supplementary Figure 15a). Second, we compare the total energy of the initial and final product of the polymerization via carbons #2, which was found to be thermodynamically unfavourable, in good agreement with the experimental evidence (Supplemenatry Figure 15b). Finally, we show the initial and final product of a hypothetic polymerization of intermediates $S2_a,$ after the first C-H cleavage, which was also found to be thermodynamically unfavorable (Supplementary Figure 15c).

Driven by the –CH termini, owing to structural parity reasons, the expected resonant form for even-membered and odd-membered polymers presents a striking difference since the odd ones should display a radical. It is well known from polyacetylene physics that under such circumstances, in principle, the radical could be delocalized over the longitudinal edge of the polymer where the bond length alternation should be strongly diminished (Figure 1 and Supplementary Figure 8)[38]. To assess the electronic differences between even- and odd-membered polymers, we probed their electronic structure by STS, complemented by DFT. Constant-height STM images acquired at low bias voltages for 10-membered and 9-membered naphthoindenylidene polymers (see Figure 4a and 4e, respectively) allow us to discern a bright contrast distributed along the polyacetylene backbone for the odd-membered polymer, which is not observed for even-membered polymers of any length (Supplementary Figures 17a-f for comparison between odd- and even-polymers of distinct length). The differential conductance d*I*/d*V* spectra on the 10-membered polymer show resonances at -0.81 V, 0.34 V, and 0.83 V (see Figure 4c, in which additional minor peaks are assigned to tip states as displayed in Supplementary Figure 18). In order to track any latent resonances, we took a ramp of d*I*/d*V* maps in steps of 50 meV from -2 eV to 2 eV (selected d*I*/d*V* maps are depicted in Figure 4d). Following such approach we could observe a hidden resonance at -0.55 V, which is tentatively assigned to the HOMO of the polymer (marked by clarity in Figure 4c). The other resonances are attributed to the HOMO-1, LUMO and LUMO +1, respectively. Simulated d*I*/d*V* maps using

DFT-calculated frontier molecular orbitals of a free-standing polymer (Figure 4d and Supplementary Figure 19) match very well the experimental results, ratifying our rationalization of the electronic structure. Reproducing this protocol, we could observe a reduction of the HOMO-LUMO gap from 2.34 eV for a dimer to 0.52 eV for an 18-membered polymer (Figure 4i,k). Next, we focused on a 9-membered polymer (Figure 4g). We identify four resonances below and above Fermi level, respectively, which we assigned to HOMO-1 (-0.80 V), HOMO (-0.55 V), LUMO (0.60 V) and LUMO+1 (1.23 V) based on a very good agreement with calculated d*I*/d*V* maps (Figure 4h). In addition, the 9-membered polymer features a strong and broad resonance crossing the Fermi level, which we attributed to an in-gap soliton state. The origin of this state emanates from the resonant structure of the odd-membered polyacetylene backbone illustrated in Figure 1, as introduced by Heeger et al. for the field of conducting polymers[38,39]. Furthermore, to investigate the energy level alignment of the soliton with respect to the polymer length, we conducted high-resolution STS measurements (Supplementary Figure 20), observing that the soliton peak slightly shifts towards more negative bias as the polymer length increases, though still crossing Fermi level. Importantly, the polymers discussed in the paper exhibit homogeneous chemical integrity. On rare occasions, we have measured extra-hydrogenated polymers. The presence of an extra hydrogen is easily detected in high-resolution nc-AFM images as a bright protrusion (Supplementary Figure 6). Such presence modifies the chemical resonant form of the polymer, and this, of course, induces the location of the soliton in certain segments of the polymer, upon specific extra-hydrogenation (Supplementary Figure 6c).

To discard the presence of a Kondo resonance at the Fermi level, we performed inelastic electron tunneling spectroscopy (IETS) with a Nickelocene functionalized tip[40]. Our results reveal no modification of the nickelocene spin excitation with varying tip-sample distances (Supplementary Figure 21). This observation indicates quenching of the radical character of the soliton state. We attribute this to the emergence of the mixed valence regime due to the Fermi level pinning caused by charge transfer between metallic substrate and molecule. This charge transfer from the polymer to the Au(111) surface is also confirmed by DFT calculations (Supplementary Figure 22). The emergence of the mixed-valence regime and the absence of the radical character of the soliton state is also supported by a numerical many-body model of polymer/surface interface (for details, see SI and Supplementary Figures 23-25). According to the model, when the soliton state approaches to the Fermi level, the charge transfer is accompanied by quenching of the radical character of the soliton state (Supplementary Figure 25).

Notably, for sufficiently long polymers, the band gap converges to a relatively low band gap value of ~0.4 eV for both even and odd-membered polymers (Figures 4i-4k). Particularly, a decrease of HOMO-LUMO gap is observed from 2.27 eV for a trimer to 0.42 eV for a 25-membered polymer (Figures 4j and 4k; note that the additional peak close to Fermi in the positive bias voltage region is assigned to a tip state as displayed in Supplementary Figure 18). Importantly, the low intrinsic band gap has a significant impact on the spatial delocalization of the soliton state. Such delocalization is illustrated in Figure 5 for the longest polymers we could measure without perturbation from the STM tip, i.e., a 21-membered polymer consisting of a polyacetylene longitudinal backbone with 63 carbons (Supplementary Figure 26 for soliton delocalization on polymers of distinct length). Both experimental and theoretical results demonstrate the strong delocalization of the soliton over the whole longitudinal polyacetylene backbone of the polymer. To appreciate this effect, we conduct a theoretical comparison of soliton delocalization among different free-standing polymers (Supplementary Figures 27-29). This analysis encompasses a prototypical polyacetylene (**10**), along with derivatives from the acenoindenylidene polymer family (**11**, **12** and **3**), all of them featuring polyacetylene longitudinal chains, while increasing the monomer size. Herein, the delocalization of the soliton state over the polymer non-linearly increases with the decreasing value of the band gap (Supplementary Figure 29). The large delocalization of the soliton state is highly remarkable and points towards novel avenues for engineering generations of highly conducting polymers by on-surface synthesis of π-conjugated nanomaterials that exhibit giant delocalization of quasiparticles.

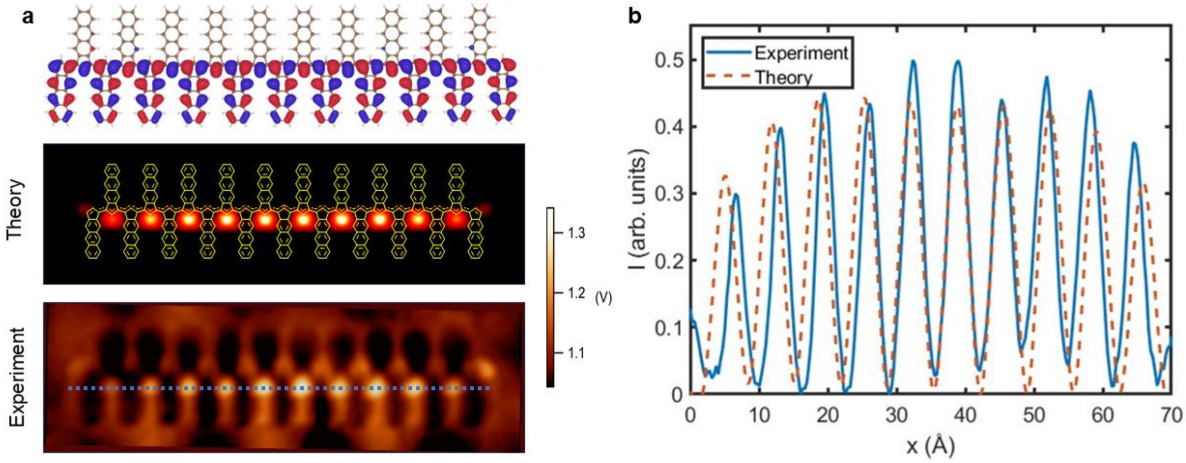

Figure 4 | High delocalization of the soliton in polymer 3o. a, Top panel, soliton wave-function of a 21-membered polymer obtained from DFT PBE0 calculations. In the middle panel, the calculated d*I*/d*V* map corresponding to the soliton wave function is shown above, along with a superimposed chemical sketch of the polymer. The bottom panel, experimental d*I*/d*V* map, was acquired near Fermi for a 21-membered polymer (V_b = -80 mV, I_t = 70 pA, V_{rms}= 20 mV). **b**, Comparison of experimental and theoretical line profile of d*I*/d*V* signal along the axis of the 21-membered polymer showing strong delocalization of the soliton state across the polymer. The line profiles are taken from the experimental (blue line) and theoretical (red dotted line) d*I*/d*V* images shown in panel **a**.

CONCLUSIONS

In summary, we report the on-surface synthesis of low-bandgap naphthoindenylidene polymers through a reaction based on the regio- and stereo-selective indenyl coupling of naphthoindane building blocks. The experimental and theoretical rationalization of the electronic structure of the polymer reveals a relatively low electronic bandgap of a few hundred meVs. Importantly, we establish the experimental relation between the structural parity of a polymer and the emergence of the highly relevant quasiparticle soliton for its conductivity. Consequently, odd-membered polymers feature a highly delocalized in-gap soliton state over the whole longitudinal backbone of the polymer, spanning a record value of delocalization of tens of carbon atoms. Our findings open avenues for developing on-surface chemistry and designing π-conjugated nanomaterials, while exemplifying a frequently forgotten aspect to consider for designing π-conjugated polymers, namely its structural parity. We envision that our results will contribute to fabricating polymers with intrinsic enhanced quasiparticle delocalization, which is of importance for the emergence of very high conductivity in plastic electronics.

Methods

STM and nc-AFM experiments

Experiments were performed in custom-designed ultra-high vacuum systems (base pressure below 5 x 10^{-10} mbar) hosting commercial low-temperature microscopes with STM/AFM capabilities from Scienta Omicron and SPECS. The Au(111) substrate (MaTeck GmbH) was cleaned by repeated cycles of Ar^+ ion sputtering (E = 1.5 keV) and subsequent annealing to 740 K for 10 minutes. All STM images shown were taken in constant-current mode, unless otherwise noted, with electrochemically etched tungsten, at a sample temperature of 4.3 K (Omicron) and 4.2 K (SPECS), respectively. Scanning parameters are specified in each figure caption. Molecular precursor **1**, was thermally sublimed onto the clean Au(111) surface kept at room temperature with a typical deposition rate of 0.5 Å/min (sublimation temperatures of 80 °C). The surface temperature was measured by a thermocouple contact on the sample plate.

Non-contact AFM measurements were performed with a tungsten tip attached to a Qplus tuning fork sensor. The tip was a posteriori functionalized by a controlled adsorption of a single CO molecule at the tip apex from a previously CO-dosed surface. The sensors were driven at their resonance frequency (26 kHz) with a constant amplitude of ~80 pm with Scienta Omicron instruments. The frequency shift from resonance of the sensor (with the attached CO-functionalized tip) was recorded in a constant-height mode (Omicron Matrix electronics and MFLi PLL by Zurich Instruments for Omicron. The STM and nc-AFM images were analyzed using WSxM [41].

Computational details

For the characterization of the C-H cleavage processes of the precursor, we carried out free-energy calculations using the Fireball/Amber[33] QM/MM method that describes the forces between the atoms in the system as a combination of classical force fields using Amber[42] and local orbital DFT provided by Fireball[43]. To describe the classical or MM part, we employed the interface force-field[44], and the DFT calculations were performed at the BLYP level[45,46] including the dispersion corrections with the D3 formalism[47].

To obtain the free energy activation barriers shown in this work, we used a combination of the Umbrella Sampling (US) method [48] and Steered Molecular Dynamics (SMD)[49]. After performing a free molecular dynamics calculation at 500K using a Langevin thermostat[50], we used SMD calculation to generate a trajectory along the reaction coordinate. Then, the frames along this trajectory were used as seeds for the different sampling windows of the US calculation.

For all the US calculations, we used the distance between the hydrogen atom to be cleaved from the molecule and the carbon atom with which this hydrogen is bonded. Along this reaction coordinate, we used 70 umbrella sampling windows from 0.8 Å to 4.3 Å, resulting in a window width of 0.05 Å. At each of these windows, 10000 MD steps at 500K were performed with a time step of 0.5 fs. Then, the Weighted Histogram Analysis Method (WHAM)[51] was used to calculate the free energy profiles.

The CI-NEB calculations carried out to find the minimum energy path of the proposed dimerization process were carried out using the aimsChain string method implemented in the FHI-AIMS package[34]. The proposed reaction paths were extrapolated from the relaxed initial final and intermediate structures relaxed with FHI-AIMS on a one-layer Au(111) substrate with an 8x6 supercell, except the system shown in Figure S15b, were a 11x4 supercell was used. At least 6 images along the path were optimized, using the string method, until the force convergence threshold of $0.1 \ {}^{eV}\!/_{\text{Å}}$ was reached. Then, the climbing image method was used to find the transition estate within the same force convergence threshold. The force convergence threshold for the second step of the process shown in Figure S15a had to be set at $0.2\ {}^{eV}/_{\text{Å}}$, to reach a reasonable convergence in an affordable time.

The geometry optimizations were done using the FHI-AIMS, at the GGA-PBE level of the theory, with energy and force tolerances of 10^{-5} eV and 10^{-2} eV/Å, respectively, light wavefunctions and the Tkatchenko-Scheffler treatment of the van der Waals interaction[52].

Simulated AFM images were obtained by AFM-Probe Particle code[53], where the probe particle had a stiffness of 0.24 N/m and a charge coefficient of -0.2e. The electrostatic interaction between the tip and sample was calculated using the Hartree potential obtained from the total DFT calculations using the FHI-AIMS package of free-standing polymers.

Calculated d*I*/d*V* maps were obtained using STM-Probe Particle code [54] for the optimized free-standing polymers using FH-AIMS PBE calculations, where CO-tip was mimicked by a probe composed of 10% s-orbital and 90% of px,py orbitals.

The analysis of soliton delocalization, presented in Figure 4 and Figures S27-S29, is based on the total energy calculations of free-standing polymers using FHI-AIMS code and PBE0 XC-functional [55].

Data and Code Availability

The datasets generated during and/or analyzed during the current study are available at IMDEA Nanoscience repository (https://repositorio.imdeananociencia.org/home).

Code Availability

The Fireball software package is available at https://github.com/fireball-QMD and the PP-SPM software package can be downloaded at https://github.com/Probe-Particle/ppafm#probe-particle-model. FHi-aims code is a commercial package available upon the requests from developers. The Amber code and the necessary post-processing tools are available for non-commercial use at the website of the Amber project: https://ambermd.org/index.php.

Acknowledgements

This project has received funding from MCIN/AEI/10.13039/501100011033 through grants PID2019-108532GB-I00, PID2022-139933NB-I00 and PID2022-140845OB-C62. We acknowledge the support from the ‘(MAD2D-CM)-IMDEA-Nanociencia’ project funded by Comunidad de Madrid, by the Recovery, Transformation and Resilience Plan, and by NextGenerationEU from the European Union. We thank support from the European Regional Development Fund of the European Union (EU) from Xunta de Galicia (Centro de Investigación de Galicia accreditation 2019–2022, ED431G 2019/03) and Xunta de Galicia-Gain Oportunius Program. We appreciate funding from the CzechNanoLab Research Infrastructure supported by MEYS CR (LM2018110) and project GACR no. 23-05486S. J.I.U. acknowledges the European Union’s Horizon 2020 research and innovation programme under the Marie Skłodowska-Curie grant agreement No [886314]. J.J. and B.A. thank the Agencia Estatal de Investigación for the award of pre-doctoral fellowships (PRE2020-092897 and BES-2017-079748, respectively). A.G. and A.B. acknowledges financial support from Juan de la Cierva program.

Author contributions

J.I.U., P.J., D.P. and D.E. conceived the project. D.E. coordinated the research efforts. K.B., A.B., O.S., A.P.-S, K.L, J.M.G., R.M., J.I.U. and D.E. acquired and analyzed the experimental data. A.G., M.L., D.S.-P. and P.J. performed the calculations. J.J., B.A., Do.P. and D.P. designed and synthesized the molecular precursor. K.B., J.I.U., P.J., D.P. and D.E. wrote the manuscript with contributions from the rest of authors.

Correspondence and requests for materials should be addressed to Jose I. Urgel (jose-ignacio.urgel@imdea.org), Pavel Jelinek (jelinekp@fzu.cz), Diego Peña (diego.pena@usc.es), or David Ecija (david.ecija@imdea.org).

Competing interests

The authors declare no competing interests.

Figure captions

Figure 1 | Solution synthesis of precursor 1 and on-surface synthesis of polymer 3. a, Delocalization of a soliton in a π-conjugated polymer simply by chemical design. **b**, Scheme of the polymerization of **1** into polymer **3** by on-surface synthesis through the formation and homocoupling of intermediate **2** upon adsorption on Au(111) held at room temperature and subsequent annealing to 200 ºC. **c**, Solution synthesis of precursor **1**. DCM stands for dichloromethane, TMS for trimethylsilyl, TfO for trifluoromethanesulfonate, TBAF for tetrabutylammonium fluoride, and TMSCl for trimethylsilyl chloride.

Figure 2 | On-surface synthesis of polymer 3 on Au(111). a, Overview STM image of a Au(111) surface after the deposition of a submonolayer coverage of **1** and subsequent annealing to 200 °C. V_b = 0.5 V, I_t = 10 pA, scale bar = 20 nm. **b**, Constant-current high-resolution STM images of polymers **3** with varying length acquired with a CO-functionalized tip. V_b = 50 mV, I_t = 50 pA (2 units); V_b = 0.3 V, I_t = 100 pA (3 units); V_b = 5 mV, I_t = 10 pA (4 units); V_b = -0.1 V, I_t = 70 pA (5 units); V_b = 5 mV, I_t = 10 pA (6 units); V_b = 0.5 V, I_t = 50 pA (7 units); V_b = 50 mV, I_t = 50 pA (8 units); V_b = 0.5 V, I_t = 50 pA (9 units); V_b = 5 mV, I_t = 10 pA (10 units); scale bars = 1 nm. **c-d**, Histograms of the abundance of the polymers regarding their length and structural parity, respectively. **e**, Constant-current STM image of the largest observed defect-free polymer comprising 86 monomers. V_b = 0.5 V, I_t = 50 pA, scale bar = 5 nm. **f**, High-resolution STM image, acquired with a CO-functionalized tip, of a dodecamer. V_b = 5 mV, I_t = 50 pA, scale bar = 1 nm. **g**, Constant-height frequency-shift nc-AFM image of **f** acquired with a CO-functionalized tip. V_b = 5 mV, 50 pA, scale bar = 1 nm. **h**, High-resolution STM image of an isolated heptamer. V_b = 500 mV, I_t = 50 pA, scale bar = 1 nm. **i,** Constant-height frequency-shift nc-AFM image of **h** acquired with a CO-functionalized tip. V_b = 10 mV, 50 pA, scale bar = 1 nm.

Figure 3 | Most favorable reaction pathways for the C-H cleavage of precursor 1 after its deposition and the posterior polymerization of intermediate 2. **a**-**c**, Initial, transitional, and final structures of the three C-H cleavage processes, respectively. **d**, Concatenation of the three free energy barriers calculated for the three C-H cleavage processes. **e**, CI-NEB calculated potential energy profile for the three step-wise polymerization process found to be more favorable, and side and top view of the calculated initial (S_i), intermediate (S_{int}) final (S_f) and transitional $(TS_{1-a}, TS_{1-b}\ and\ TS_2)$ states.

Figure 4 | Electronic structure of polymer 3 with respect to its structural parity. a,**e**, Constant-height high-resolution STM images of an even-membered (10-membered) and an odd-membered (9-membered) polymers acquired with a CO-functionalized tip. V_b = 5 mV, scale bars = 1 nm. **b**,**f**, High-resolution STM images of a 10-membered and 9-membered polymers acquired with a CO-functionalized tip, respectively. V_b = −2.0 V, I_t = 100 pA; scale bars = 1 nm. **c**,**g**, d*I*/d*V* spectra of 10-membered and 9-membered polymers acquired at the positions indicated by the colored circles in **b**,**f**. Reference spectra taken on the bare Au(111) surface are depicted in orange, and the acquisition position is marked with an orange circle. Open feedback parameters for d*I*/d*V* spectra: V_b = −2.0 V, I_t = 100 pA, V_{rms} = 20 mV. **d**,**h**, Top panel, experimental constant-current d*I*/d*V* maps acquired with a CO-tip. **d**, HOMO (V_b = −0.56 V, I_t = 250 pA) and LUMO (V_b = 0.25 V, I_t = 250 pA), with V_{rms} = 20 mV for a 10-membered polymer; **h**, HOMO (V_b = −0.5 V, I_t = 250 pA), Soliton (V_b = −0.10 V, I_t = 70 pA), and LUMO (V_b = 0.60 V, I_t = 250 pA), V_{rms} = 20 mV.Middle panel, corresponding DFT-calculated maps (tip-sample height = 5 Å) at the energy positions of the frontier orbitals. Bottom panel, electronic wavefunctions of the distinct states from DFT calculations. **i**,**j**, d*I*/d*V* spectra of even- and odd-membered polymers of distinct lengths, respectively. Inset: Chemical scheme showing the acquisition positions of the spectra by a colored circle. **k,** Graph displaying the evolution of HOMO-LUMO gaps of the polymers as a function of their length.

Figure 5 | High delocalization of the soliton in polymer 3o. a, Top panel, soliton wave-function of a 21-membered polymer obtained from DFT PBE0 calculations. In the middle panel, the calculated d*I*/d*V* map corresponding to the soliton wave function is shown above, along with a superimposed chemical sketch of the polymer. The bottom panel, experimental d*I*/d*V* map, was acquired near Fermi for a 21-membered polymer (V_b = -80 mV, I_t = 70 pA, V_{rms}= 20 mV). **b**, Comparison of experimental and theoretical line profile of d*I*/d*V* signal along the axis of the 21-membered polymer showing strong delocalization of the soliton state across the polymer. The line profiles are taken from the experimental (blue line) and theoretical (red dotted line) d*I*/d*V* images shown in panel **a**.

References

1. Heeger, A.J. Semiconducting and Metallic Polymers: The Fourth Generation of Polymeric Materials (Nobel Lecture). *Angew. Chem. Int. Ed.* **40**, 2591-2611 (2001).
2. K, N. & Rout, C.S. Conducting polymers: a comprehensive review on recent advances in synthesis, properties and applications. *RSC Advances* **11**, 5659-5697 (2021).
3. Polarons, Solitons, Excitons, and Conducting Polymers in *Foundations of Solid State Physics* 301-401 (2019).
4. Facchetti, A. π-Conjugated Polymers for Organic Electronics and Photovoltaic Cell Applications. *Chem. Mater.* **23**, 733-758 (2011).
5. Guo, X., Baumgarten, M. & Müllen, K. Designing π-conjugated polymers for organic electronics. *Prog. Polym. Sci.* **38**, 1832-1908 (2013).
6. Oka, K., Winther-Jensen, B. & Nishide, H. Organic π-Conjugated Polymers as Photocathode Materials for Visible-Light-Enhanced Hydrogen and Hydrogen Peroxide Production from Water. *Adv. Energy Mat.* **11**, 2003724 (2021).
7. Shen, Q., Gao, H.-Y. & Fuchs, H. Frontiers of on-surface synthesis: From principles to applications. *Nano Today* **13**, 77-96 (2017).
8. Clair, S. & de Oteyza, D.G. Controlling a Chemical Coupling Reaction on a Surface: Tools and Strategies for On-Surface Synthesis. *Chem. Rev.* **119**, 4717-4776 (2019).
9. Sun, Q., Zhang, R., Qiu, J., Liu, R. & Xu, W. On-Surface Synthesis of Carbon Nanostructures. *Adv. Mat.* **30**, 1705630 (2018).
10. Gu, Y., Qiu, Z. & Müllen, K. Nanographenes and Graphene Nanoribbons as Multitalents of Present and Future Materials Science. *J. Am. Chem. Soc.* **144**, 11499-11524 (2022).
11. Song, S. *et al.* On-surface synthesis of graphene nanostructures with π-magnetism. *Chem. Soc. Rev.* **50**, 3238-3262 (2021).
12. Mishra, S. *et al.* Large magnetic exchange coupling in rhombus-shaped nanographenes with zigzag periphery. *Nat. Chem.* **13**, 581-586 (2021).
13. Biswas, K. *et al.* Steering Large Magnetic Exchange Coupling in Nanographenes near the Closed-Shell to Open-Shell Transition. *J. Am. Chem. Soc.* **145**, 2968-2974 (2023).
14. Sánchez-Grande, A. *et al.* On-surface synthesis of ethynylene bridged anthracene polymers. *Angew. Chem. Int. Ed.* **58**, 6559-6563 (2019).
15. Cirera, B. *et al.* Tailoring topological order and pi-conjugation to engineer quasi-metallic polymers. *Nat. Nanotechnol.* **15**, 437-443 (2020).
16. Sánchez-Grande, A. *et al.* Surface-Assisted Synthesis of N-Containing π-Conjugated Polymers. *Adv. Sci.* **9**, 2200407 (2022).
17. Cai, J. *et al.* Atomically precise bottom-up fabrication of graphene nanoribbons. *Nature* **466**, 470-473 (2010).
18. Talirz, L., Ruffieux, P. & Fasel, R. On-Surface Synthesis of Atomically Precise Graphene Nanoribbons. *Adv. Mat.* **28**, 6222-6231 (2016).
19. Rizzo, D.J. *et al.* Topological band engineering of graphene nanoribbons. *Nature* **560**, 204-208 (2018).

20. Gröning, O. *et al.* Engineering of robust topological quantum phases in graphene nanoribbons. *Nature* **560**, 209-213 (2018).
21. Moreno, C. *et al.* Bottom-up synthesis of multifunctional nanoporous graphene. *Science* **360**, 199 (2018).
22. Fan, Q. *et al.* Biphenylene network: A nonbenzenoid carbon allotrope. *Science* **372**, 852-856 (2021).
23. Weiss, C. *et al.* Imaging Pauli Repulsion in Scanning Tunneling Microscopy. *Phys. Rev. Lett.* **105**, 086103 (2010).
24. Gross, L. *et al.* Atomic Force Microscopy for Molecular Structure Elucidation. *Angew. Chem. Int. Ed.* **57**, 3888-3908 (2018).
25. Zhang, C., Yi, Z. & Xu, W. Scanning probe microscopy in probing low-dimensional carbon-based nanostructures and nanomaterials. *Mater. Futures* **1**, 032301 (2022).
26. Hernangómez-Pérez, D., Gunasekaran, S., Venkataraman, L. & Evers, F. Solitonics with Polyacetylenes. *Nano Lett.* **20**, 2615-2619 (2020).
27. Shi, J., Li, L. & Li, Y. o-Silylaryl Triflates: A Journey of Kobayashi Aryne Precursors. *Chem. Rev.* **121**, 3892-4044 (2021).
28. Riss, A. *et al.* Local Electronic and Chemical Structure of Oligo-acetylene Derivatives Formed Through Radical Cyclizations at a Surface. *Nano Letters* **14**, 2251-2255 (2014).
29. Écija, D. *et al.* Crossover site-selectivity in the adsorption of the fullerene derivative PCBM on Au(111). *Angew. Chem. Int. Ed.* **46**, 7874-7877 (2007).
30. Gross, L., Mohn, F., Moll, N., Liljeroth, P. & Meyer, G. The Chemical Structure of a Molecule Resolved by Atomic Force Microscopy. *Science* **325**, 1110 (2009).
31. Gross, L. *et al.* Bond-order discrimination by atomic force microscopy. *Science* **337**, 1326-9 (2012).
32. Biswas, K. *et al.* Interplay between π-Conjugation and Exchange Magnetism in One-Dimensional Porphyrinoid Polymers. *J. Am. Chem. Soc.* **144**, 12725-12731 (2022).
33. Mendieta-Moreno, J.I. *et al.* fireball/amber: An Efficient Local-Orbital DFT QM/MM Method for Biomolecular Systems. *J. Chem. Theory Comput.* **10**, 2185-2193 (2014).
34. E, W., Ren, W. & Vanden-Eijnden, E. Simplified and improved string method for computing the minimum energy paths in barrier-crossing events. *J. Chem. Phys.* **126** (2007).
35. Liu, X. *et al.* Exploiting Cooperative Catalysis for the On-Surface Synthesis of Linear Heteroaromatic Polymers via Selective C–H Activation. *Angew. Chem. Int. Ed.* **61**, e202112798 (2022).
36. Mendieta-Moreno, J.I. *et al.* Unusual Scaffold Rearrangement in Polyaromatic Hydrocarbons Driven by Concerted Action of Single Gold Atoms on a Gold Surface. *Angew. Chem. Int. Ed.* **61**, e202208010 (2022).
37. Lowe, B. *et al.* Selective Activation of Aromatic C–H Bonds Catalyzed by Single Gold Atoms at Room Temperature. *J. Am. Chem. Soc.* **144**, 21389-21397 (2022).
38. Heeger, A.J., Kivelson, S., Schrieffer, J.R. & Su, W.P. Solitons in conducting polymers. *Rev. Mod. Phys.* **60**, 781-850 (1988).
39. Wang, S. *et al.* On-surface synthesis and characterization of individual polyacetylene chains. *Nat. Chem.* **11**, 924-930 (2019).
40. Verlhac, B. *et al.* Atomic-scale spin sensing with a single molecule at the apex of a scanning tunneling microscope. *Science* **366**, 623-627 (2019).
41. Horcas, I. *et al.* WSxM: a software for scanning probe microscopy and a tool for nanotechnology. *Rev. Sci. Instrum.* **78**, 013705 (2007).
42. Case, D.A. AMBER 2018. (2018).

43. Lewis, J.P. *et al.* Advances and applications in the FIREBALL ab initio tight-binding molecular-dynamics formalism. *Phys. Status Solidi B* **248**, 1989-2007 (2011).
44. Heinz, H., Lin, T.-J., Kishore Mishra, R. & Emami, F.S. Thermodynamically Consistent Force Fields for the Assembly of Inorganic, Organic, and Biological Nanostructures: The INTERFACE Force Field. *Langmuir* **29**, 1754-1765 (2013).
45. Becke, A.D. Density-functional thermochemistry. III. The role of exact exchange. *J. Chem. Phys.* **98**, 5648 (1998).
46. Lee, C., Yang, W. & Parr, R.G. Development of the Colle-Salvetti correlation-energy formula into a functional of the electron density. *Phys. Rev. B* **37**, 785-789 (1988).
47. Grimme, S., Ehrlich, S. & Goerigk, L. Effect of the damping function in dispersion corrected density functional theory. *J. Comput. Chem.* **32**, 1456-1465 (2011).
48. Darve, E. & Pohorille, A. Calculating free energies using average force. *J. Chem. Phys.* **115**, 9169-9183 (2001).
49. Izrailev, S. *et al.* Steered Molecular Dynamics. in *Computational Molecular Dynamics: Challenges, Methods, Ideas* (eds Deuflhard, P. *et al.*) 39-65 (Springer Berlin Heidelberg, Berlin, Heidelberg, 1999).
50. Pastor, R.W., Brooks, B.R. & Szabo, A. An analysis of the accuracy of Langevin and molecular dynamics algorithms. *Mol. Phys.* **65**, 1409-1419 (1988).
51. Kumar, S., Rosenberg, J.M., Bouzida, D., Swendsen, R.H. & Kollman, P.A. THE weighted histogram analysis method for free-energy calculations on biomolecules. I. The method. *J. Comput. Chem.* **13**, 1011-1021 (1992).
52. Tkatchenko, A. & Scheffler, M. Accurate Molecular Van Der Waals Interactions from Ground-State Electron Density and Free-Atom Reference Data. *Physical Review Letters* **102**, 073005 (2009).
53. Hapala, P. *et al.* Mechanism of high-resolution STM/AFM imaging with functionalized tips. *Phys. Rev. B* **90**, 085421 (2014).
54. Krejčí, O., Hapala, P., Ondráček, M. & Jelínek, P. Principles and simulations of high-resolution STM imaging with a flexible tip apex. *Phys. Rev. B* **95**, 045407 (2017).
55. Perdew, J.P., Ernzerhof, M. & Burke, K. Rationale for mixing exact exchange with density functional approximations. *J. Chem. Phys.* **105**, 9982-9985 (1996).